EUROPEAN ORGANIZATION FOR NUCLEAR RESEARCH

CERN-PH-EP/2005-011
March 4, 2005

Compton Scattering of Quasi-Real Virtual Photons at LEP

L3 Collaboration

Abstract

Compton scattering of quasi-real virtual photons, $\gamma e^{\pm} \to \gamma e^{\pm}$, is studied with 0.6 fb^{-1} of data collected by the L3 detector at the LEP e^+e^- collider at centre-of-mass energies $\sqrt{s} = 189 - 209$ GeV. About 4500 events produced by the interaction of virtual photons emitted by $e^{\pm}$ of one beam with $e^{\mp}$ of the opposite beam are collected for effective centre-of-mass energies of the photon-electron and photon-positron systems in the range from $\sqrt{s'} = 35$ GeV up to $\sqrt{s'} = 175$ GeV, the highest energy at which Compton scattering was ever probed. The cross sections of the $\gamma e^{\pm} \to \gamma e^{\pm}$ process as a function of $\sqrt{s'}$ and of the rest-frame scattering angle are measured, combined with previous L3 measurements down to $\sqrt{s'} \simeq 20$ GeV, and found to agree with the QED expectations.

Submitted to *Phys. Lett. B*

1 Introduction

The CERN LEP e^+e^- collider allowed high-energy tests of high-order QED through the detection of events with multiple hard-photon production [1] and the study of lepton pairs produced by two-photon interactions [2].

A unique test of QED at e^+e^- colliders is the study of Compton scattering, $\gamma e^\pm \to \gamma e^\pm$. In this process, quasi-real virtual photons[1)] emitted by one of the incoming beams interact with the electrons[2)] of the other beam. This process, $e^+e^- \to e^+e^-\gamma$, is sketched in Figure 1. The electron which radiates the quasi-real photon is scattered at a very small angle and escapes detection along the beam pipe. The signature of such a process is a photon and an electron in the detector, with a large amount of missing momentum directed along the beam line. The $\gamma e^\pm \to \gamma e^\pm$ process is characterised by the effective centre-of-mass energy of the photon-electron collision, $\sqrt{s'}$, and by the scattering angle of the electron in the photon-electron centre-of-mass system, θ^*, shown in Figure 1. At the lowest order, the differential cross section as a function of $\cos\theta^*$ is [3]:

$$\frac{\mathrm{d}\sigma}{\mathrm{d}\cos\theta^*} = \frac{\alpha^2\pi}{s'}\left(\frac{1+\cos\theta^*}{2} + \frac{2}{1+\cos\theta^*}\right), \tag{1}$$

where α is the fine-structure constant. In the angular range $|\cos\theta^*| < 0.8$, this corresponds to a cross section of about 200 pb at $\sqrt{s'} = 40$ GeV and of about 20 pb at $\sqrt{s'} = 130$ GeV.

Quasi-real Compton scattering in e^+e^- colliders was first discussed more than three decades ago [4] and observed at the 900 MeV ACO storage ring in Orsay [5]. The L3 Collaboration studied this process at e^+e^- centre-of-mass energies $\sqrt{s} = 91 - 183$ GeV, covering with high statistics the effective centre-of-mass energy range $\sqrt{s'} = 20 - 100$ GeV [6]. This Letter presents the extension of this analysis to the high-luminosity and high-energy data sample collected at LEP at $\sqrt{s} = 189 - 209$ GeV with the L3 detector [7–9]. This data sample comprises 0.6 fb^{-1} of integrated luminosity, as detailed in Table 1. It extends the accessible $\sqrt{s'}$ range to about 175 GeV, allowing to probe Compton scattering at energies never attained before.

2 Event simulation

The TEEGG Monte Carlo [10] is used to simulate the $e^+e^- \to e^+e^-\gamma$ process with one electron scattered in the angular range $|\cos\theta| > 0.996$ and both the other electron and the photon in the angular range $|\cos\theta| < 0.985$. The $\sqrt{s'}$ spectrum for the $\gamma e^\pm \to \gamma e^\pm$ process generated by TEEGG was compared [11] with the QED expectations obtained by convolving the QED cross section with the virtual-photon flux modelled with the equivalent-photon approach [12]. The two spectra agree within the expected statistical precision of this measurement.

The following Monte Carlo programs are used to model the background processes: BHWIDE [13] for Bhabha scattering, $e^+e^- \to e^+e^-$, KK2f [14] for tau pair-production, $e^+e^- \to \tau^+\tau^-$, GGG [15] for multi-photon production, $e^+e^- \to \gamma\gamma(\gamma)$, and DIAG36 [16] for electron pair-production in two-photon collisions, $e^+e^- \to e^+e^-e^+e^-$.

Large samples of Monte Carlo events are generated at each e^+e^- centre-of-mass energy. The number of simulated signal events corresponds to at least thirty times the number of expected

[1)] A "quasi-real" virtual photon is one whose virtuality, $Q^2 = -m_\gamma^2$, is much smaller than all relevant scales of the process and is therefore kinematically equivalent to a real photon with $Q^2 = 0$.

[2)] In this Letter, the term "electron" is in general used to refer to both electrons and positrons, unless specified otherwise.

data events. For background processes, this factor varies from six times for Bhabha scattering, up to more than one hundred times for the $e^+e^- \to \tau^+\tau^-$ process.

The L3 detector response is simulated using the GEANT program [17], which takes into account the effects of energy loss, multiple scattering and showering in the detector. Time-dependent efficiencies of the different subdetectors, as monitored during the data-taking period, are taken into account in the simulation procedure. The simulated events are reconstructed with the same program used for the data.

3 Reconstruction of event kinematics

A crucial part of the measurement is the determination of $\sqrt{s'}$ and $\cos\theta^*$. These are inferred with high precision by imposing the constraints that there are only three particles in the final state and one of the electrons is directed along the beam line. The polar angles of the observed electron and photon, θ_e and θ_γ, defined in Figure 1, are used to calculate the missing energy, $E_{\rm miss}$, as:

$$E_{\rm miss} = \sqrt{s}\frac{|\sin(\theta_e+\theta_\gamma)|}{\sin\theta_e+\sin\theta_\gamma+|\sin(\theta_e+\theta_\gamma)|}.$$

The square of the effective centre-of-mass energy of the $\gamma e^\pm \to \gamma e^\pm$ process is then:

$$s' = s\left(1-2\frac{E_{\rm miss}}{\sqrt{s}}\right).$$

Monte Carlo studies show that the resolution on $\sqrt{s'}$ is better than 500 MeV. This improves by 30% the resolution obtained if only the energies of the measured particles are used. The resolution on the measured energies of the electron, E_e, and of the photon E_γ is also improved by re-calculating these quantities with the kinematic constraints:

$$E_e^{\rm angle} = \sqrt{s}\frac{\sin\theta_\gamma}{\sin\theta_e+\sin\theta_\gamma+|\sin(\theta_e+\theta_\gamma)|},$$

$$E_\gamma^{\rm angle} = \sqrt{s}\frac{\sin\theta_e}{\sin\theta_e+\sin\theta_\gamma+|\sin(\theta_e+\theta_\gamma)|}.$$

Both $E_e^{\rm angle}$ and $E_\gamma^{\rm angle}$ have a resolution of about 200 MeV. The cosine of the scattering angle of the electron in the electron-photon centre-of-mass system is:

$$\cos\theta^* = \frac{\sin(\theta_\gamma-\theta_e)}{\sin\theta_\gamma+\sin\theta_e}.$$

The resolution on $\cos\theta^*$ in Monte Carlo events is found to be better than 0.005.

4 Event selection

Events from Compton scattering must have one track in the central tracker and two clusters in the BGO electromagnetic calorimeter in the fiducial volume $|\cos\theta| < 0.96$. The clusters must have energies of at least 5 GeV and the lateral profile of their showers must match that expected for electromagnetic showers. One of these clusters must be associated to the track, which should be reconstructed from at least 80% of the hits along its sensitive track-length. This cluster is identified as the electron.

The low polar-angle regions of the L3 detector are instrumented with two calorimeters. The first is composed of BGO crystals and is used to detect Bhabha scattering in order to measure the luminosity [8]. It covers the angular region $1.4^\circ < \theta < 3.9^\circ$. The second is built from lead and plastic scintillators and extends this angular coverage up to 9° [9]. The sum of the energies deposited in these two calorimeters, E_{forward}, is required to be less than 50 GeV, as shown in Figure 2a. This cut ensures that no electron is detected above 1.4° and therefore only the scattering of quasi-real photons is considered.

After these pre-selection requirements, about 36500 events are observed in data and 32500 are expected from Monte Carlo processes, of which 18% is due to signal and 82% to background. The main source of background is Bhabha scattering with a high-energy initial-state-radiation (ISR) photon emitted in the beam pipe, which gives the missing-energy signature, and an electron which mimics a photon. Electrons are misidentified as photons more frequently in data than in Monte Carlo, which results in the excess of observed events over the Monte Carlo prediction. An additional contribution to this background comes from tau pair-production where both taus decay into electrons, one of which is identified as a photon, and the four neutrinos are responsible for the missing-energy signature. A lesser source of background is the production of events with three photons, where one of the photons escapes detection along the beam line and another, through photon conversion, is mistaken for an electron. Several additional criteria are devised to cope with these background sources.

Bhabha scattering and multi-photon production favour events with electromagnetic clusters which are back-to-back in space. These background sources are strongly reduced by a cut on the angle between the two clusters, $\zeta < 2.8$ rad, as illustrated in Figure 2b.

Events from tau pair-production are suppressed by requiring $E_{\mathrm{e}}/E_{\mathrm{e}}^{\mathrm{angle}} > 0.7$ if $E_{\mathrm{e}} > E_\gamma$ or $E_\gamma/E_\gamma^{\mathrm{angle}} > 0.7$ otherwise, as shown in Figure 2c. This cut enforces the three-particle hypothesis and rejects events where the missing momentum is not directed along the beam axis.

The analysis is restricted to $\sqrt{s'} > 35$ GeV, as displayed in Figure 2d, in order to exclude the region L3 measured with high statistics [6] and concentrate on the high-energy data.

The background from Bhabha scattering is mainly concentrated in the forward scattering region, $\cos\theta^* > 0.8$, as presented in Figure 2e. This region is removed from the analysis. The backward-scattering region, $\cos\theta^* < -0.8$, is also removed in order to reduce the systematic uncertainty from a wrong assignment of the electron charge.

The contribution from Bhabha scattering to the selected events is further inspected. In the forward scattering region, $0.4 < \cos\theta^* < 0.8$, the background electrons are mostly emitted in the central regions of the detector, as shown in Figure 2f. This follows from the emission of a hard ISR photon. This background is further reduced by requiring the electron to satisfy $|\cos\theta_{\mathrm{e}}| > 0.6$ if $0.4 < \cos\theta^* < 0.8$.

After these cuts, 4487 events are selected in data and 4534 are expected from Monte Carlo simulations, as detailed in Table 1 [18]. Background processes are estimated to contribute to about 3.5% of this sample. Two thirds of the background is due to Bhabha scattering, one quarter to electron production in two photon collisions and the rest to multi-photon production and tau pair-production. The distributions of the energies and the angles of the electrons and photons of the selected events are shown in Figures 3a–d. Figure 3e presents the normalised sum of the momenta of the electron and photon along the beam line, $|p_{\mathrm{z}}|/\sqrt{s}$. As expected, a large boost along the beam line is observed. Figure 3f shows the rapidity of the selected events.

Monte Carlo studies indicate that the average value of Q^2 for the selected events is 0.48 GeV^2 and 90% of the photons satisfy $Q^2 < 2$ GeV^2. This corresponds to a small average-virtuality

$\langle Q^2/s' \rangle \simeq 3 \times 10^{-3}$, which justifies the treatment of the virtual photons as quasi-real ones. The kinematics of the process under investigation is such that $p_{\rm t}^2 \simeq Q^2$, where $p_{\rm t}$ is the sum of the momenta of the final state electron and photon in the plane transverse to the beams. Figure 4a shows the distribution of $p_{\rm t}^2$ for the selected events. An average value $< p_{\rm t}^2 >= 0.3$ GeV^2 is observed, with a root-mean-square of 1 GeV^2, which further validates the hypothesis of quasi-real photons.

The distribution of $\cos\theta^*$ for the selected events, shown in Figure 4b, presents the characteristic backward-scattering behaviour of Compton scattering. Figure 4c displays the observed and expected distributions of $\sqrt{s'}$. The average value of $\sqrt{s'}$ is 64 GeV. Ten events are observed in data for $\sqrt{s'} > 163$ GeV, up to $\sqrt{s'} = 175$ GeV, the largest energies at which Compton scattering was ever observed. Monte Carlo simulations predict 9 ± 1 events in this region, with a background of 7%. The uncertainty is due to the limited statistics of the generated Monte Carlo sample. Figure 4 presents one of these high-energy events.

5 Systematic uncertainties

Several sources of systematic uncertainty are considered and their impact on the measurement of the cross section as a function of $\sqrt{s'}$ and of the differential cross section as a function of $\cos\theta^*$ are listed in Table 2.

The measurement of the photon and electron angles is crucial to the determination of the event kinematics. These variables are smeared by $\pm 1\%$ to account for possible uncertainties in detector alignment, time-dependent changes in resolution or discrepancies between the data and the Monte Carlo simulations. The effects of these changes are larger for events with large values of $\sqrt{s'}$ or $\cos\theta^*$. In addition, the energy scale of the electromagnetic calorimeter is varied within its uncertainty of $\pm 1\%$. As the energies are mainly inferred from the angular measurements, this change has a small impact on the cross sections.

The amount of charge confusion in the tracker is measured with control data-samples and is well reproduced in the Monte Carlo simulations. However, uncertainties in this simulation are a potential source of systematics. This is assessed by injecting in the simulations an additional amount of charge confusion. A small variation in the cross section as a function of $\sqrt{s'}$ is observed, whereas a larger uncertainty affects the determination of the differential cross section for large values of $\cos\theta^*$.

Uncertainties of the background normalisation are also propagated to the final results. All background levels are varied by $\pm 2\%$ with the exception of electron production in two-photon collisions, varied by $\pm 10\%$.

Finally, the effects of the limited amount of signal and background Monte Carlo statistics are treated as additional systematic uncertainties.

6 Results

The phase space covered by this analysis, 35 GeV $< \sqrt{s'} <$ 175 GeV and $-0.8 < \cos\theta^* < 0.8$, is divided in ten intervals in $\sqrt{s'}$ and twelve intervals in $\cos\theta^*$. The limits of these intervals are detailed in Tables 3 and 4, together with their average values[3)] and the numbers of observed and expected events, also shown in Figures 4b and 4c.

[3)] The average values are calculated as suggested in Reference 19.

The differential cross section of the $e^+e^- \to e^+e^-\gamma$ process as a function of $\sqrt{s'}$ is related to the cross section of the $\gamma e^\pm \to \gamma e^\pm$ process by:

$$\frac{d\sigma_{e^+e^-\to e^+e^-\gamma}}{d\sqrt{s'}} = f_\gamma(\sqrt{s}, \sqrt{s'})\, \sigma_{\gamma e^\pm \to \gamma e^\pm}(\sqrt{s'}), \tag{2}$$

where $f_\gamma(\sqrt{s}, \sqrt{s'})$ is the virtual-photon flux. The cross section of the $e^+e^- \to e^+e^-\gamma$ process for the i-th interval of $\sqrt{s'}$ can be extracted from the numbers of events observed in data and expected from signal and background Monte Carlo simulations, $N_{\rm data}(i)$, $N^{\rm sign}_{\rm MC}(i)$ and $N^{\rm back}_{\rm MC}(i)$, respectively, as:

$$\frac{\Delta\sigma_{e^+e^-\to e^+e^-\gamma}}{\Delta\sqrt{s'}} = \frac{\Delta\sigma^{\rm MC}_{e^+e^-\to e^+e^-\gamma}}{\Delta\sqrt{s'}} \frac{N_{\rm data}(i) - N^{\rm back}_{\rm MC}(i)}{N^{\rm sign}_{\rm MC}(i)}, \tag{3}$$

where $\Delta\sigma^{\rm MC}_{e^+e^-\to e^+e^-\gamma}/\Delta\sqrt{s'}$ is the cross section predicted by the Monte Carlo. By expressing Equation 3 in terms of Equation 2, and assuming that $f_\gamma(\sqrt{s}, \sqrt{s'})$ is the same for data and Monte Carlo, the cross section for quasi-real Compton scattering at the average effective centre-of-mass energy $\langle\sqrt{s'}\rangle$ can be derived directly from the values in Table 3 as:

$$\sigma_{\gamma e^\pm \to \gamma e^\pm}\left(\langle\sqrt{s'}\rangle\right) = \sigma^{\rm QED}_{\gamma e^\pm \to \gamma e^\pm}\left(\langle\sqrt{s'}\rangle\right) \frac{N_{\rm data}(i) - N^{\rm back}_{\rm MC}(i)}{N^{\rm sign}_{\rm MC}(i)}, \tag{4}$$

where $\sigma^{\rm QED}_{\gamma e^\pm \to \gamma e^\pm}\left(\langle\sqrt{s'}\rangle\right)$ is the value expected from QED. The differential cross section for quasi-real Compton scattering as a function of $\cos\theta^*$ is derived from a formula equivalent to Equation 4, *mutatis mutandis*.

The selected events are further classified according to the presence of either electrons or positrons in the final states. The cross section as a function of $\sqrt{s'}$ and the differential cross section as a function of $\cos\theta$ are measured and the results are presented in Figures 6a and 6b. They are in good mutual agreement. The combined results for electrons and positrons are presented in Tables 3 and 4 and in Figures 6c and 6d. All results are in good agreement with the QED predictions, also presented in Tables 3 and 4 and in Figure 6. The predictions for the cross section as a function of $\sqrt{s'}$ are derived by integrating Equation 1 over the range $-0.8 < \cos\theta^* < 0.8$, while the predictions for the differential cross section as a function of $\cos\theta$ are derived by integrating over the range 35 GeV $< \sqrt{s'} <$ 175 GeV.

The cross sections as a function of $\sqrt{s'}$ measured in the range $\sqrt{s'} = 35 - 175$ GeV are combined with those L3 measured in the range $\sqrt{s'} = 20 - 100$ GeV [6]. The full data-sample collected by the L3 detector at $\sqrt{s} = 91 - 209$ GeV is therefore considered, covering a range $\sqrt{s'} = 20 - 175$ GeV. The results are presented in Table 5 and Figure 7. They are in good agreement, over two orders of magnitude, with the QED predictions.

References

[1] ALEPH Collab., A. Heister *et al.*, Eur. Phys. J. **C 28** (2003) 1;
DELPHI Collab., J. Abdallah *et al.*, Eur. Phys. J. **C 37** (2004) 405;
L3 Collab, P. Achard *et al.*, Phys. Lett. **B 531** (2002) 28;
OPAL Collab, G. Abbiendi *et al.* Eur. Phys. J. **C 26** (2003) 331.

[2] DELPHI Collab., J. Abdallah *et al.*, Eur. Phys. J. **C 35** (2004) 159;
L3 Collab., P. Achard *et al.*, Phys. Lett. **B 585** (2004) 53.

[3] F. Halzen and A.D. Martin, *Quarks & Leptons* (Wiley, New York, 1984).

[4] C. Carimalo, P. Kessler and J. Parisi, Nucl. Phys. **B 57** (1973) 582.

[5] G. Cosme *et al.*, Lett. Nuovo Cimento **8** (1973) 509.

[6] L3 Collab., M. Acciarri *et al.*, Phys. Lett. **B 439** (1998) 183.

[7] L3 Collab., B. Adeva *et al.*, Nucl. Instr. Meth. **A 289** (1990) 35;
L3 Collab., O. Adriani *et al.*, Phys. Rep. **236** (1993) 1;
J.A. Bakken *et al.*, Nucl. Instr. Meth. **A 275** (1989) 81;
O. Adriani *et al.*, Nucl. Instr. Meth. **A 302** (1991) 53;
B. Adeva *et al.*, Nucl. Instr. Meth. **A 323** (1992) 109;
K. Deiters *et al.*, Nucl. Instr. Meth. **A 323** (1992) 162;
M. Acciarri *et al.*, Nucl. Instr. Meth. **A 351** (1994) 300;
G. Basti *et al.*, Nucl. Instr. Meth. **A 374** (1996) 293.

[8] I.C. Brock *et al.*, Nucl. Instr. Meth. **A 381** (1996) 236.

[9] M. Chemarin *et al.*, Nucl. Instr. Meth. **A 349** (1994) 345.

[10] TEEGG version 7.1 is used;
D. Karlen, Nucl. Phys. **B 289** (1987) 23.

[11] A.S. Schmidt-Kärst, *Elektron-Photon Physik bei LEP*, Ph.D. thesis, RWTH Aachen, 2000.

[12] V.M. Budnev *et al.,* Phys. Rep. **15** (1975) 181.

[13] BHWIDE version 1.03 is used;
S. Jadach, W. Placzek and B.F.L. Ward, Phys. Lett. **B 390** (1997) 298.

[14] KK2f version 4.13 is used;
S. Jadach, B.F.L. Ward and Z. Wąs, Comp. Phys.Comm. **130** (2000) 260.

[15] GGG Monte Carlo;
F.A. Berends and R. Kleiss, Nucl. Phys. **B 186** (1981) 22.

[16] DIAG36 Monte Carlo;
F.A. Berends, P.H. Daverfeldt, R. Kleiss, Nucl. Phys. **B 253** (1985) 441.

[17] GEANT version 3.15 is used;
R. Brun *et al.*, preprint CERN DD/EE/84-1 (1985), revised 1987.

[18] R. Vasquez, *Study of single Z-boson production and Compton scattering in electron-positron collisions at LEP at centre-of-mass energies up to* 209 GeV, Ph.D. thesis, Purdue University, 2005.

[19] G.D. Lafferty and T.R. Wyatt, Nucl. Instr. Meth. **A 355** (1995) 541.

The L3 Collaboration:

P.Achard,[20] O.Adriani,[17] M.Aguilar-Benitez,[25] J.Alcaraz,[25] G.Alemanni,[23] J.Allaby,[18] A.Aloisio,[29] M.G.Alviggi,[29] H.Anderhub,[49] V.P.Andreev,[6,34] F.Anselmo,[8] A.Arefiev,[28] T.Azemoon,[3] T.Aziz,[9] P.Bagnaia,[39] A.Bajo,[25] G.Baksay,[26] L.Baksay,[26] S.V.Baldew,[2] S.Banerjee,[9] Sw.Banerjee,[4] A.Barczyk,[49,47] R.Barillère,[18] P.Bartalini,[23] M.Basile,[8] N.Batalova,[46] R.Battiston,[33] A.Bay,[23] F.Becattini,[17] U.Becker,[13] F.Behner,[49] L.Bellucci,[17] R.Berbeco,[3] J.Berdugo,[25] P.Berges,[13] B.Bertucci,[33] B.L.Betev,[49] M.Biasini,[33] M.Biglietti,[29] A.Biland,[49] J.J.Blaising,[4] S.C.Blyth,[35] G.J.Bobbink,[2] A.Böhm,[1] L.Boldizsar,[12] B.Borgia,[39] S.Bottai,[17] D.Bourilkov,[49] M.Bourquin,[20] S.Braccini,[20] J.G.Branson,[41] F.Brochu,[4] J.D.Burger,[13] W.J.Burger,[33] X.D.Cai,[13] M.Capell,[13] G.Cara Romeo,[8] G.Carlino,[29] A.Cartacci,[17] J.Casaus,[25] F.Cavallari,[39] N.Cavallo,[36] C.Cecchi,[33] M.Cerrada,[25] M.Chamizo,[20] Y.H.Chang,[44] M.Chemarin,[24] A.Chen,[44] G.Chen,[7] G.M.Chen,[7] H.F.Chen,[22] H.S.Chen,[7] G.Chiefari,[29] L.Cifarelli,[40] F.Cindolo,[8] I.Clare,[13] R.Clare,[38] G.Coignet,[4] N.Colino,[25] S.Costantini,[39] B.de la Cruz,[25] S.Cucciarelli,[33] R.de Asmundis,[29] P.Déglon,[20] J.Debreczeni,[12] A.Degré,[4] K.Dehmelt,[26] K.Deiters,[47] D.della Volpe,[29] E.Delmeire,[20] P.Denes,[37] F.DeNotaristefani,[39] A.De Salvo,[49] M.Diemoz,[39] M.Dierckxsens,[2] C.Dionisi,[39] M.Dittmar,[49] A.Doria,[29] M.T.Dova,[10,♯] D.Duchesneau,[4] M.Duda,[1] B.Echenard,[20] A.Eline,[18] A.El Hage,[1] H.El Mamouni,[24] A.Engler,[35] F.J.Eppling,[13] P.Extermann,[20] M.A.Falagan,[25] S.Falciano,[39] A.Favara,[32] J.Fay,[24] O.Fedin,[34] M.Felcini,[49] T.Ferguson,[35] H.Fesefeldt,[1] E.Fiandrini,[33] J.H.Field,[20] F.Filthaut,[31] P.H.Fisher,[13] W.Fisher,[37] I.Fisk,[41] G.Forconi,[13] K.Freudenreich,[49] C.Furetta,[27] Yu.Galaktionov,[28,13] S.N.Ganguli,[9] P.Garcia-Abia,[25] M.Gataullin,[32] S.Gentile,[39] S.Giagu,[39] Z.F.Gong,[22] G.Grenier,[24] O.Grimm,[49] M.W.Gruenewald,[16] M.Guida,[40] V.K.Gupta,[37] A.Gurtu,[9] L.J.Gutay,[46] D.Haas,[5] D.Hatzifotiadou,[8] T.Hebbeker,[1] A.Hervé,[18] J.Hirschfelder,[35] H.Hofer,[49] M.Hohlmann,[26] G.Holzner,[49] S.R.Hou,[44] B.N.Jin,[7] P.Jindal,[14] L.W.Jones,[3] P.de Jong,[2] I.Josa-Mutuberría,[25] M.Kaur,[14] M.N.Kienzle-Focacci,[20] J.K.Kim,[43] J.Kirkby,[18] W.Kittel,[31] A.Klimentov,[13,28] A.C.König,[31] M.Kopal,[46] V.Koutsenko,[13,28] M.Kräber,[49] R.W.Kraemer,[35] A.Krüger,[48] A.Kunin,[13] P.Ladron de Guevara,[25] I.Laktineh,[24] G.Landi,[17] M.Lebeau,[18] A.Lebedev,[13] P.Lebrun,[24] P.Lecomte,[49] P.Lecoq,[18] P.Le Coultre,[49] J.M.Le Goff,[18] R.Leiste,[48] M.Levtchenko,[27] P.Levtchenko,[34] C.Li,[22] S.Likhoded,[48] C.H.Lin,[44] W.T.Lin,[44] F.L.Linde,[2] L.Lista,[29] Z.A.Liu,[7] W.Lohmann,[48] E.Longo,[39] Y.S.Lu,[7] C.Luci,[39] L.Luminari,[39] W.Lustermann,[49] W.G.Ma,[22] L.Malgeri,[18] A.Malinin,[28] C.Maña,[25] J.Mans,[37] J.P.Martin,[24] F.Marzano,[39] K.Mazumdar,[9] R.R.McNeil,[6] S.Mele,[18,29] L.Merola,[29] M.Meschini,[17] W.J.Metzger,[31] A.Mihul,[11] H.Milcent,[18] G.Mirabelli,[39] J.Mnich,[1] G.B.Mohanty,[9] G.S.Muanza,[24] A.J.M.Muijs,[2] B.Musicar,[41] M.Musy,[39] S.Nagy,[15] S.Natale,[20] M.Napolitano,[29] F.Nessi-Tedaldi,[49] H.Newman,[32] A.Nisati,[39] T.Novak,[31] H.Nowak,[48] R.Ofierzynski,[49] G.Organtini,[39] I.Pal,[46] C.Palomares,[25] P.Paolucci,[29] R.Paramatti,[39] G.Passaleva,[17] S.Patricelli,[29] T.Paul,[10] M.Pauluzzi,[33] C.Paus,[13] F.Pauss,[49] M.Pedace,[39] S.Pensotti,[27] D.Perret-Gallix,[4] D.Piccolo,[29] F.Pierella,[8] M.Pioppi,[33] P.A.Piroué,[37] E.Pistolesi,[27] V.Plyaskin,[28] M.Pohl,[20] V.Pojidaev,[17] J.Pothier,[18] D.Prokofiev,[34] G.Rahal-Callot,[49] M.A.Rahaman,[9] P.Raics,[15] N.Raja,[9] R.Ramelli,[49] P.G.Rancoita,[27] R.Ranieri,[17] A.Raspereza,[48] P.Razis,[30] D.Ren,[49] M.Rescigno,[39] S.Reucroft,[10] S.Riemann,[48] K.Riles,[3] B.P.Roe,[3] L.Romero,[25] A.Rosca,[48] C.Rosemann,[1] C.Rosenbleck,[1] S.Rosier-Lees,[4] S.Roth,[1] J.A.Rubio,[18] G.Ruggiero,[17] H.Rykaczewski,[49] A.Sakharov,[49] S.Saremi,[6] S.Sarkar,[39] J.Salicio,[18] E.Sanchez,[25] C.Schäfer,[18] V.Schegelsky,[34] S.Schmidt-Kaerst,[1] H.Schopper,[21] D.J.Schotanus,[31] C.Sciacca,[29] L.Servoli,[33] S.Shevchenko,[32] N.Shivarov,[42] V.Shoutko,[13] E.Shumilov,[28] A.Shvorob,[32] D.Son,[43] C.Souga,[24] P.Spillantini,[17] M.Steuer,[13] D.P.Stickland,[37] B.Stoyanov,[42] A.Straessner,[20] K.Sudhakar,[9] G.Sultanov,[42] L.Z.Sun,[22] S.Sushkov,[1] H.Suter,[49] J.D.Swain,[10] Z.Szillasi,[26,¶] X.W.Tang,[7] P.Tarjan,[15] L.Tauscher,[5] L.Taylor,[10] B.Tellili,[24] D.Teyssier,[24] C.Timmermans,[31] Samuel C.C.Ting,[13] S.M.Ting,[13] S.C.Tonwar,[9] J.Tóth,[12] C.Tully,[37] K.L.Tung,[7] J.Ulbricht,[49] E.Valente,[39] R.T.Van de Walle,[31] R.Vasquez,[46] V.Veszpremi,[26] G.Vesztergombi,[12] I.Vetlitsky,[28] G.Viertel,[49] S.Villa,[38] M.Vivargent,[4] S.Vlachos,[5] I.Vodopianov,[26] H.Vogel,[35] H.Vogt,[48] I.Vorobiev,[35,28] A.A.Vorobyov,[34] M.Wadhwa,[5] Q.Wang,[31] X.L.Wang,[22] Z.M.Wang,[22] M.Weber,[18] S.Wynhoff,[37] L.Xia,[32] Z.Z.Xu,[22] J.Yamamoto,[3] B.Z.Yang,[22] C.G.Yang,[7] H.J.Yang,[3] M.Yang,[7] S.C.Yeh,[45] An.Zalite,[34] Yu.Zalite,[34] Z.P.Zhang,[22] J.Zhao,[22] G.Y.Zhu,[7] R.Y.Zhu,[32] H.L.Zhuang,[7] A.Zichichi,[8,18,19] B.Zimmermann,[49] M.Zöller.[1]

1 III. Physikalisches Institut, RWTH, D-52056 Aachen, Germany§
2 National Institute for High Energy Physics, NIKHEF, and University of Amsterdam, NL-1009 DB Amsterdam, The Netherlands
3 University of Michigan, Ann Arbor, MI 48109, USA
4 Laboratoire d'Annecy-le-Vieux de Physique des Particules, LAPP,IN2P3-CNRS, BP 110, F-74941 Annecy-le-Vieux CEDEX, France
5 Institute of Physics, University of Basel, CH-4056 Basel, Switzerland
6 Louisiana State University, Baton Rouge, LA 70803, USA
7 Institute of High Energy Physics, IHEP, 100039 Beijing, China△
8 University of Bologna and INFN-Sezione di Bologna, I-40126 Bologna, Italy
9 Tata Institute of Fundamental Research, Mumbai (Bombay) 400 005, India
10 Northeastern University, Boston, MA 02115, USA
11 Institute of Atomic Physics and University of Bucharest, R-76900 Bucharest, Romania
12 Central Research Institute for Physics of the Hungarian Academy of Sciences, H-1525 Budapest 114, Hungary‡
13 Massachusetts Institute of Technology, Cambridge, MA 02139, USA
14 Panjab University, Chandigarh 160 014, India
15 KLTE-ATOMKI, H-4010 Debrecen, Hungary¶
16 Department of Experimental Physics, University College Dublin, Belfield, Dublin 4, Ireland
17 INFN Sezione di Firenze and University of Florence, I-50125 Florence, Italy
18 European Laboratory for Particle Physics, CERN, CH-1211 Geneva 23, Switzerland
19 World Laboratory, FBLJA Project, CH-1211 Geneva 23, Switzerland
20 University of Geneva, CH-1211 Geneva 4, Switzerland
21 University of Hamburg, D-22761 Hamburg, Germany
22 Chinese University of Science and Technology, USTC, Hefei, Anhui 230 029, China△
23 University of Lausanne, CH-1015 Lausanne, Switzerland
24 Institut de Physique Nucléaire de Lyon, IN2P3-CNRS,Université Claude Bernard, F-69622 Villeurbanne, France
25 Centro de Investigaciones Energéticas, Medioambientales y Tecnológicas, CIEMAT, E-28040 Madrid, Spain♭
26 Florida Institute of Technology, Melbourne, FL 32901, USA
27 INFN-Sezione di Milano, I-20133 Milan, Italy
28 Institute of Theoretical and Experimental Physics, ITEP, Moscow, Russia
29 INFN-Sezione di Napoli and University of Naples, I-80125 Naples, Italy
30 Department of Physics, University of Cyprus, Nicosia, Cyprus
31 Radboud University and NIKHEF, NL-6525 ED Nijmegen, The Netherlands
32 California Institute of Technology, Pasadena, CA 91125, USA
33 INFN-Sezione di Perugia and Università Degli Studi di Perugia, I-06100 Perugia, Italy
34 Nuclear Physics Institute, St. Petersburg, Russia
35 Carnegie Mellon University, Pittsburgh, PA 15213, USA
36 INFN-Sezione di Napoli and University of Potenza, I-85100 Potenza, Italy
37 Princeton University, Princeton, NJ 08544, USA
38 University of Californa, Riverside, CA 92521, USA
39 INFN-Sezione di Roma and University of Rome, "La Sapienza", I-00185 Rome, Italy
40 University and INFN, Salerno, I-84100 Salerno, Italy
41 University of California, San Diego, CA 92093, USA
42 Bulgarian Academy of Sciences, Central Lab. of Mechatronics and Instrumentation, BU-1113 Sofia, Bulgaria
43 The Center for High Energy Physics, Kyungpook National University, 702-701 Taegu, Republic of Korea
44 National Central University, Chung-Li, Taiwan, China
45 Department of Physics, National Tsing Hua University, Taiwan, China
46 Purdue University, West Lafayette, IN 47907, USA
47 Paul Scherrer Institut, PSI, CH-5232 Villigen, Switzerland
48 DESY, D-15738 Zeuthen, Germany
49 Eidgenössische Technische Hochschule, ETH Zürich, CH-8093 Zürich, Switzerland
§ Supported by the German Bundesministerium für Bildung, Wissenschaft, Forschung und Technologie.
‡ Supported by the Hungarian OTKA fund under contract numbers T019181, F023259 and T037350.
¶ Also supported by the Hungarian OTKA fund under contract number T026178.
♭ Supported also by the Comisión Interministerial de Ciencia y Tecnología.
♯ Also supported by CONICET and Universidad Nacional de La Plata, CC 67, 1900 La Plata, Argentina.
△ Supported by the National Natural Science Foundation of China.

$\sqrt{s}$ (GeV)	188.6	191.6	195.6	199.5	201.7	202.5 – 205.5	205.5 – 209.2
$\mathcal{L}$ (pb^{-1})	176.8	28.9	82.9	67.8	36.2	75.6	137.7
N_{data}	1409	221	612	460	266	545	974
N_{MC}	1336	231	659	521	284	520	982

Table 1: Integrated luminosities, $\mathcal{L}$, and numbers of events selected in data, N_{data}, and Monte Carlo, N_{MC}, at each $\mathrm{e^+e^-}$ centre-of-mass energy.

	Systematic uncertainty on	
Source	$\sigma_{\gamma\mathrm{e}^\pm\to\gamma\mathrm{e}^\pm}(\sqrt{s'})$	$\mathrm{d}\sigma_{\gamma\mathrm{e}^\pm\to\gamma\mathrm{e}^\pm}/\mathrm{d}\cos\theta^*$
Measurement of angles	0.2% – 3.8%	0.1% – 18.6%
Energy scale	0.1% – 0.9%	0.1% – 1.9%
Charge confusion	0.1% – 0.2%	0.1% – 19.8%
Background normalisation	0.1% – 0.2%	0.1% – 0.3%
Signal Monte Carlo statistics	1.0% – 3.7%	1.3% – 6.9%
Background Monte Carlo statistics	0.3% – 2.4%	0.3% – 4.2%
Total	1.3% – 5.5%	1.5% – 28.2%

Table 2: Systematic uncertainties on the cross section as a function of $\sqrt{s'}$ and of the differential cross section as a function of $\cos\theta^*$. The largest uncertainties correspond to the low-statistics high $\sqrt{s'}$ regions and to the forward-scattering regions, where angular measurements and charge confusion effects are important.

$\sqrt{s'}$ (GeV)	$\langle\sqrt{s'}\rangle$ (GeV)	$N_{\rm data}$	$N_{\rm MC}^{\rm sign}$	$N_{\rm MC}^{\rm back}$	$\sigma_{\gamma e^\pm\to\gamma e^\pm}$ (pb)	$\sigma^{\rm QED}_{\gamma e^\pm\to\gamma e^\pm}$ (pb)
35 – 45	39.7	1269	1229.7	32.0	$216.0 \pm 6.0 \pm 4.7$	214.7
45 – 55	49.7	889	900.3	22.5	$131.5 \pm 4.6 \pm 1.8$	136.7
55 – 65	59.8	627	610.6	11.8	$95.3 \pm 3.8 \pm 2.2$	94.6
65 – 75	69.8	506	472.5	9.8	$72.9 \pm 3.1 \pm 1.5$	69.4
75 – 85	79.8	370	342.4	16.5	$54.8 \pm 2.8 \pm 1.2$	53.1
85 – 100	92.2	357	346.9	14.9	$39.2 \pm 2.1 \pm 1.1$	39.8
100 – 115	107.2	205	214.4	5.8	$27.3 \pm 2.1 \pm 0.8$	29.4
115 – 130	122.3	125	138.2	2.6	$20.0 \pm 2.0 \pm 0.7$	22.6
130 – 145	137.3	87	86.6	3.3	$17.3 \pm 1.9 \pm 0.9$	17.9
145 – 175	159.3	52	66.6	6.5	$9.1 \pm 1.8 \pm 0.7$	13.3

Table 3: Number of events observed in each $\sqrt{s'}$ bin with average $\langle\sqrt{s'}\rangle$, $N_{\rm data}$, together with the signal, $N_{\rm MC}^{\rm sign}$, and background, $N_{\rm MC}^{\rm back}$, Monte Carlo predictions. The measured cross sections, $\sigma_{\gamma e^\pm\to\gamma e^\pm}$, are given with their statistical and systematic uncertainties, respectively, together with the QED predictions, $\sigma^{\rm QED}_{\gamma e^\pm\to\gamma e^\pm}$. The data sample at $\sqrt{s} = 188.6 - 209.2$ GeV is considered, and the cosine of the electron rest-frame scattering angle is limited to the range $|\cos\theta^*| < 0.8$.

$\cos\theta^*$	$\langle\cos\theta^*\rangle$	$N_{\rm data}$	$N_{\rm MC}^{\rm sign}$	$N_{\rm MC}^{\rm back}$	$\mathrm{d}\sigma_{\gamma e^\pm\to\gamma e^\pm}/\mathrm{d}\cos\theta^*$ (pb)	$\mathrm{d}\sigma^{\rm QED}_{\gamma e^\pm\to\gamma e^\pm}/\mathrm{d}\cos\theta^*$ (pb)
−0.80 – −0.67	−0.74	346	283.3	25.8	$133.8 \pm 6.4 \pm 9.6 \times 10^2$	118.3×10^2
−0.67 – −0.53	−0.60	389	385.2	15.7	$77.2 \pm 4.0 \pm 2.6 \times 10^2$	79.6×10^2
−0.53 – −0.40	−0.47	499	469.9	11.2	$63.6 \pm 2.7 \pm 2.5 \times 10^2$	61.2×10^2
−0.40 – −0.27	−0.34	553	593.5	14.5	$46.0 \pm 2.1 \pm 1.5 \times 10^2$	50.7×10^2
−0.27 – −0.13	−0.20	742	733.8	10.1	$43.1 \pm 1.6 \pm 0.7 \times 10^2$	44.1×10^2
−0.13 – 0.0	−0.07	616	650.2	7.9	$37.0 \pm 1.6 \pm 0.6 \times 10^2$	39.6×10^2
0.0 – 0.13	0.06	512	509.2	5.8	$36.4 \pm 1.6 \pm 0.6 \times 10^2$	36.6×10^2
0.13 – 0.27	0.20	353	347.6	10.9	$33.4 \pm 1.8 \pm 0.8 \times 10^2$	34.4×10^2
0.27 – 0.40	0.33	221	202.4	5.1	$35.0 \pm 2.2 \pm 2.2 \times 10^2$	32.9×10^2
0.40 – 0.53	0.46	135	126.7	11.9	$30.1 \pm 2.7 \pm 3.1 \times 10^2$	31.8×10^2
0.53 – 0.67	0.60	81	73.5	2.8	$33.1 \pm 3.4 \pm 5.9 \times 10^2$	31.1×10^2
0.67 – 0.80	0.73	40	33.1	4.1	$33.3 \pm 4.8 \pm 8.7 \times 10^2$	30.7×10^2

Table 4: Number of events observed in each $\cos\theta^*$ bin with average $\langle\cos\theta^*\rangle$, $N_{\rm data}$, together with the signal, $N_{\rm MC}^{\rm sign}$, and background, $N_{\rm MC}^{\rm back}$, Monte Carlo predictions. The measured differential cross sections, $\mathrm{d}\sigma_{\gamma e^\pm\to\gamma e^\pm}/\mathrm{d}\cos\theta^*$, are given with their statistical and systematic uncertainties, respectively, together with the QED predictions, $\mathrm{d}\sigma^{\rm QED}_{\gamma e^\pm\to\gamma e^\pm}/\mathrm{d}\cos\theta^*$. The data sample at $\sqrt{s} = 188.6 - 209.2$ GeV is considered, corresponding to an effective centre-of-mass energy range $\sqrt{s'} = 35 - 175$ GeV.

$\sqrt{s'}$(GeV)	$\langle\sqrt{s'}\rangle$(GeV)	$\sigma_{\gamma e^{\pm}\to\gamma e^{\pm}}$	$\sigma^{\rm QED}_{\gamma e^{\pm}\to\gamma e^{\pm}}$
$0-25$	21.0	771.2 ± 21.6	764.8
$25-35$	29.8	370.6 ± 11.3	381.1
$35-45$	39.7	213.2 ± 5.4	214.7
$45-55$	49.7	128.7 ± 3.9	136.7
$55-65$	59.8	95.0 ± 3.5	94.6
$65-75$	69.8	70.6 ± 2.9	69.4
$75-85$	79.8	55.2 ± 2.6	53.1
$85-100$	92.2	38.8 ± 2.2	39.8
$100-115$	107.2	27.3 ± 2.2	29.4
$115-130$	122.3	20.0 ± 2.1	22.6
$130-145$	137.3	17.3 ± 2.1	17.9
$145-175$	159.3	9.1 ± 2.0	13.3

Table 5: Measured cross sections, $\sigma_{\gamma e^{\pm}\to\gamma e^{\pm}}$, with their combined statistical and systematic uncertainties together with the QED predictions, $\sigma^{\rm QED}_{\gamma e^{\pm}\to\gamma e^{\pm}}$. The full L3 data sample at $\sqrt{s} = 91.2 - 209.2$ GeV is considered and the cosine of the electron rest-frame scattering angle is limited to the range $|\cos\theta^*| < 0.8$.

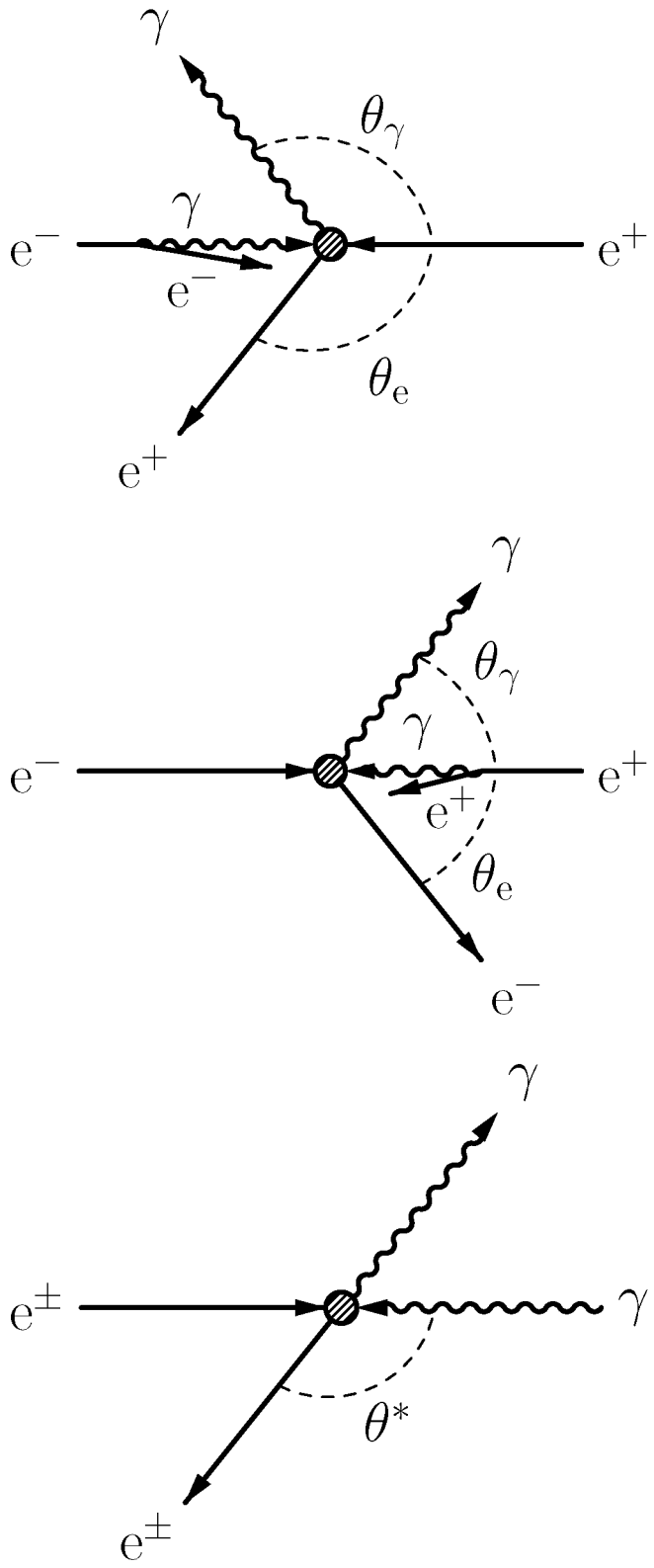

Figure 1: Schematic view of quasi-real Compton scattering in e^+e^- collisions in the laboratory system, higher plots, and in the $\gamma e^\pm$ centre-of-mass frame, lowest plot.

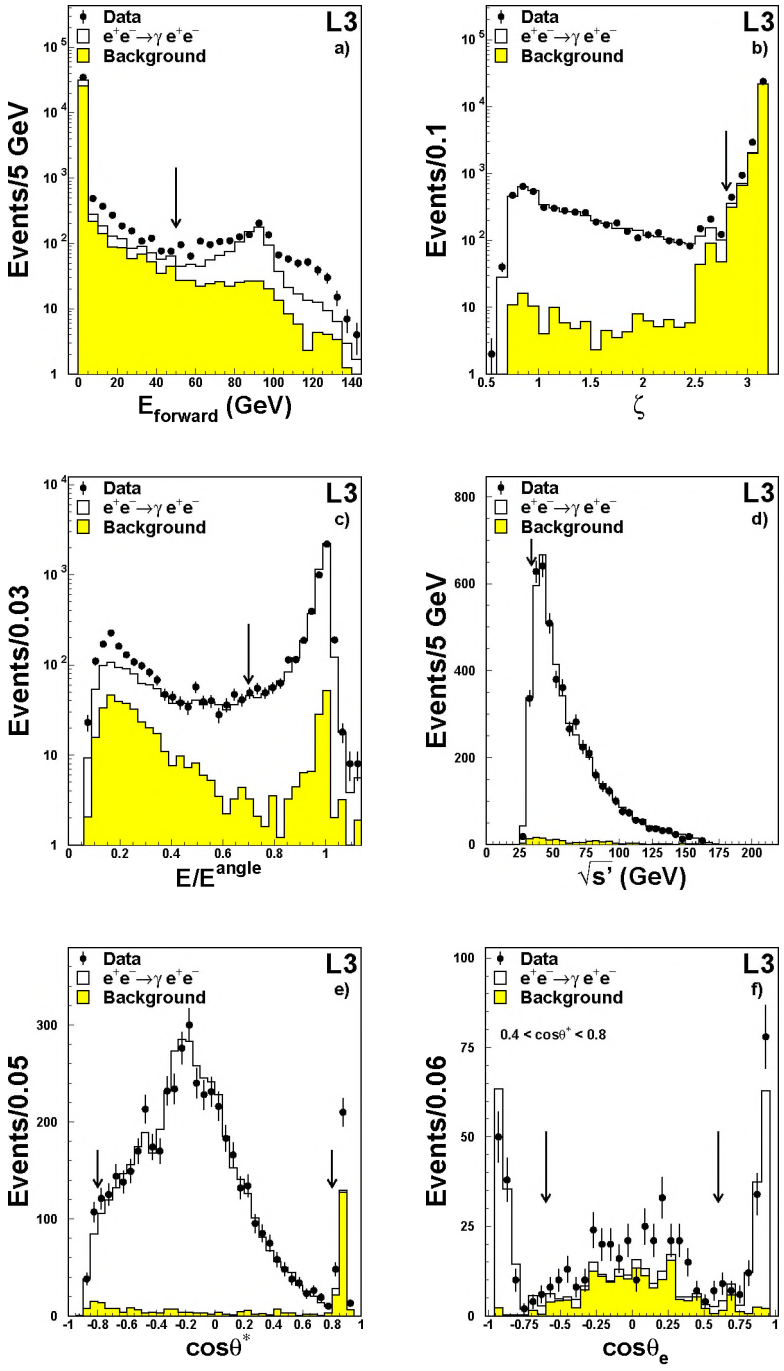

Figure 2: Distributions of some selection variables for data and Monte Carlo predictions. a) Energy in the forward calorimeters, $E_{\rm forward}$; b) angle between the electron and the photon, ζ; c) ratio of the energies of the most energetic particle as measured in the calorimeter and as obtained from the angular constraints, $E/E^{\rm angle}$; d) effective centre-of-mass energy, $\sqrt{s'}$; e) cosine of the electron scattering angle in the $\gamma e^{\pm}$ rest frame, $\cos\theta^*$; f) cosine of the polar angle of the electron, $\cos\theta_{\rm e}$, for $0.4 < \cos\theta^* < 0.8$. The arrows indicate the position of the cuts. In a) all other pre-selection cuts are applied. In b) all cuts are applied but the one on $\cos\theta^*$. In c)−f) cuts on all other variables are applied.

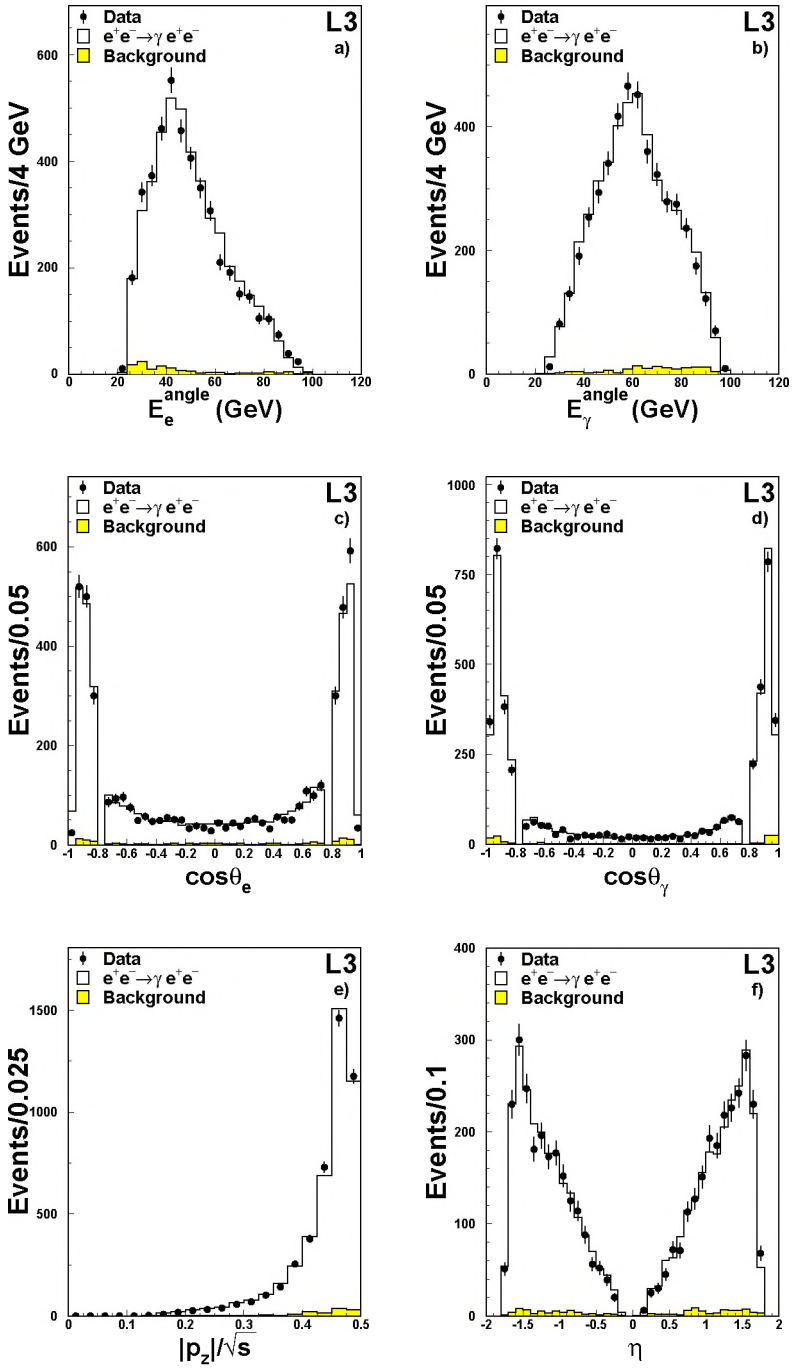

Figure 3: Distributions of variables for events selected in data and in the signal and background Monte Carlo samples. Energy of a) the electron, $E_{\mathrm{e}}^{\mathrm{angle}}$, and b) the photon, $E_{\gamma}^{\mathrm{angle}}$; cosine of the polar angle of c) the electron, θ_{e}, and d) the photon, θ_{γ}; e) normalised sum of the electron and photon longitudinal momenta, $|p_{\mathrm{z}}|/\sqrt{s}$; f) rapidity of the event, η.

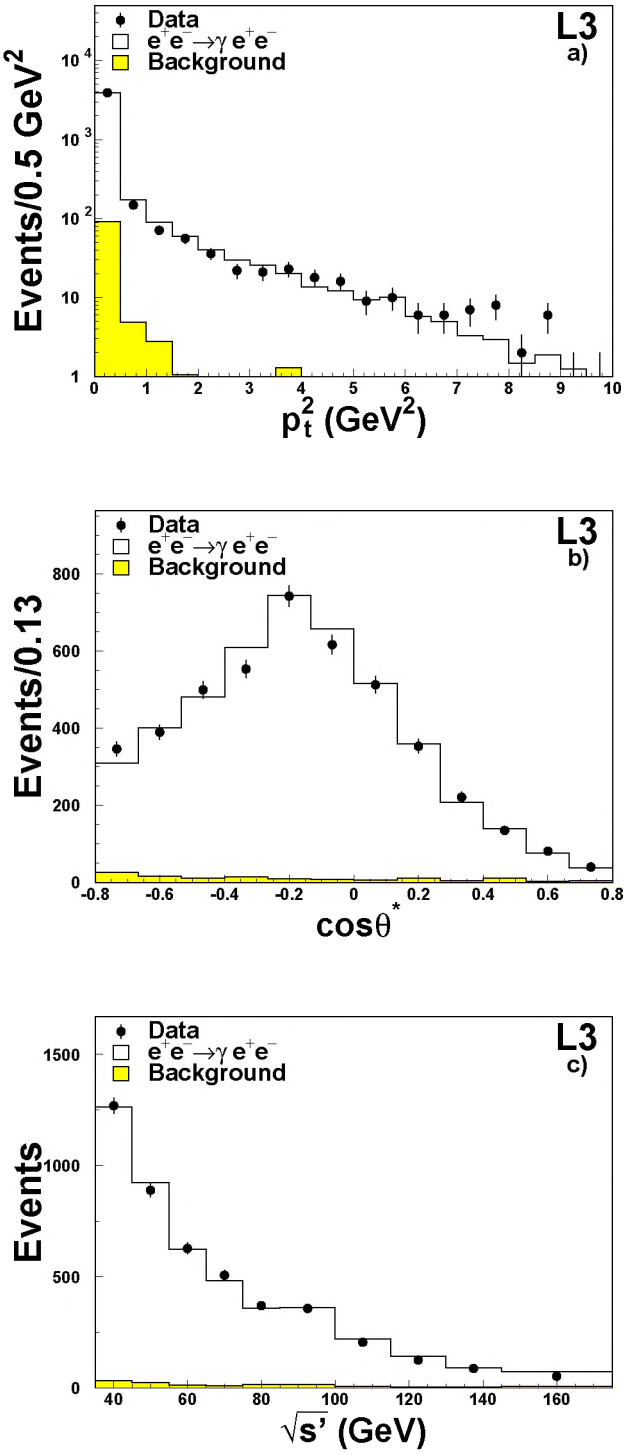

Figure 4: Distributions of variables for events selected in data and in the signal and background Monte Carlo samples. a) Square of the sum of the electron and photon transverse momenta, $p_{\rm t}^2$; b) cosine of the electron scattering angle in the $\gamma e^{\pm}$ rest frame, $\cos\theta^*$; c) effective centre-of-mass energy, $\sqrt{s'}$.

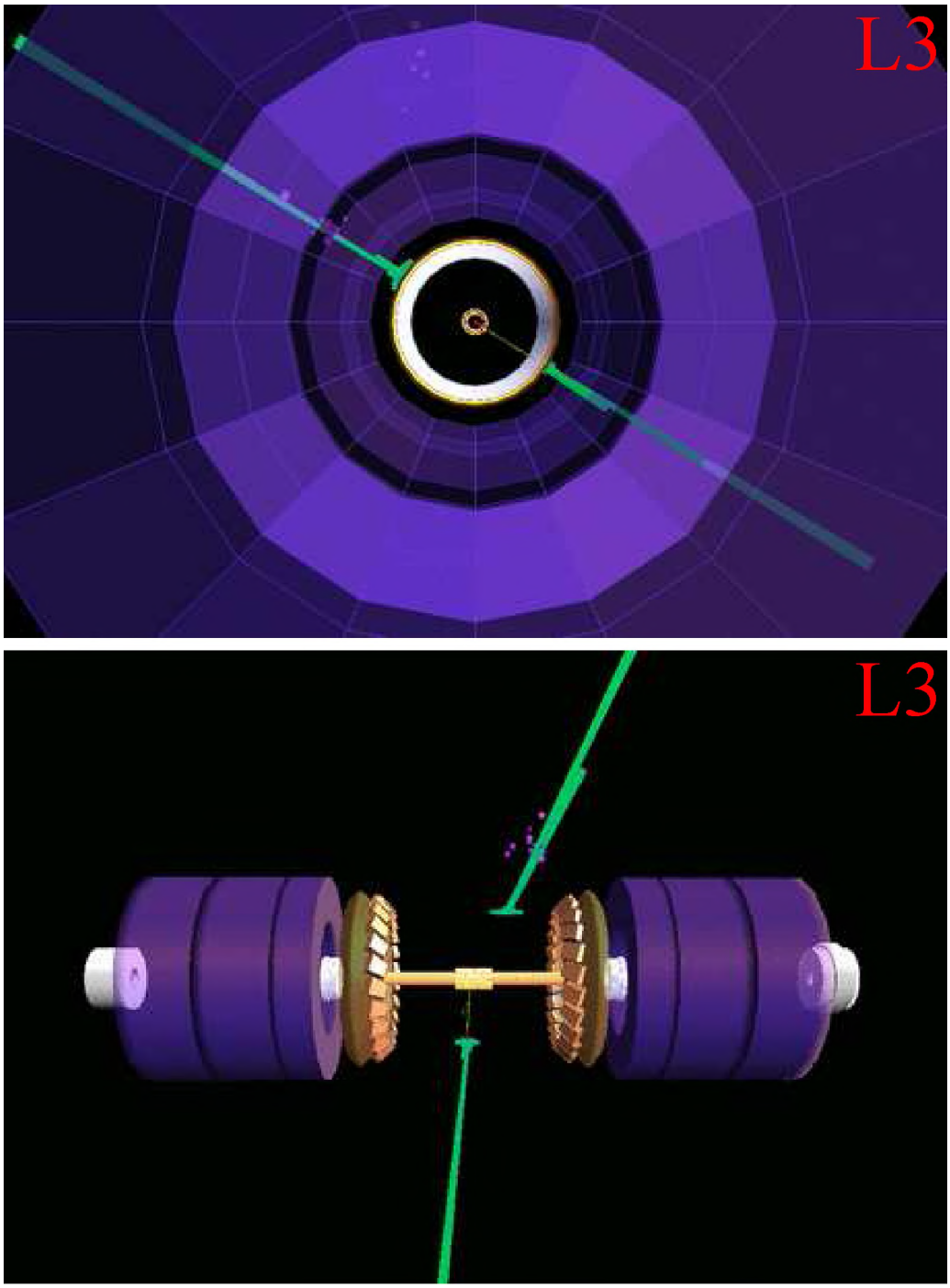

Figure 5: Views of a high-energy candidate for quasi-real Compton scattering in the plane transverse to the beams, higher plot, and in a plane along the beams, lower plot. The towers represent the energy deposited in the electromagnetic calorimeter and the boxes are low-energy clusters in the hadron calorimeter. The track of the electron is clearly visible, while no track is associated to the other electromagnetic cluster, identified as the photon.

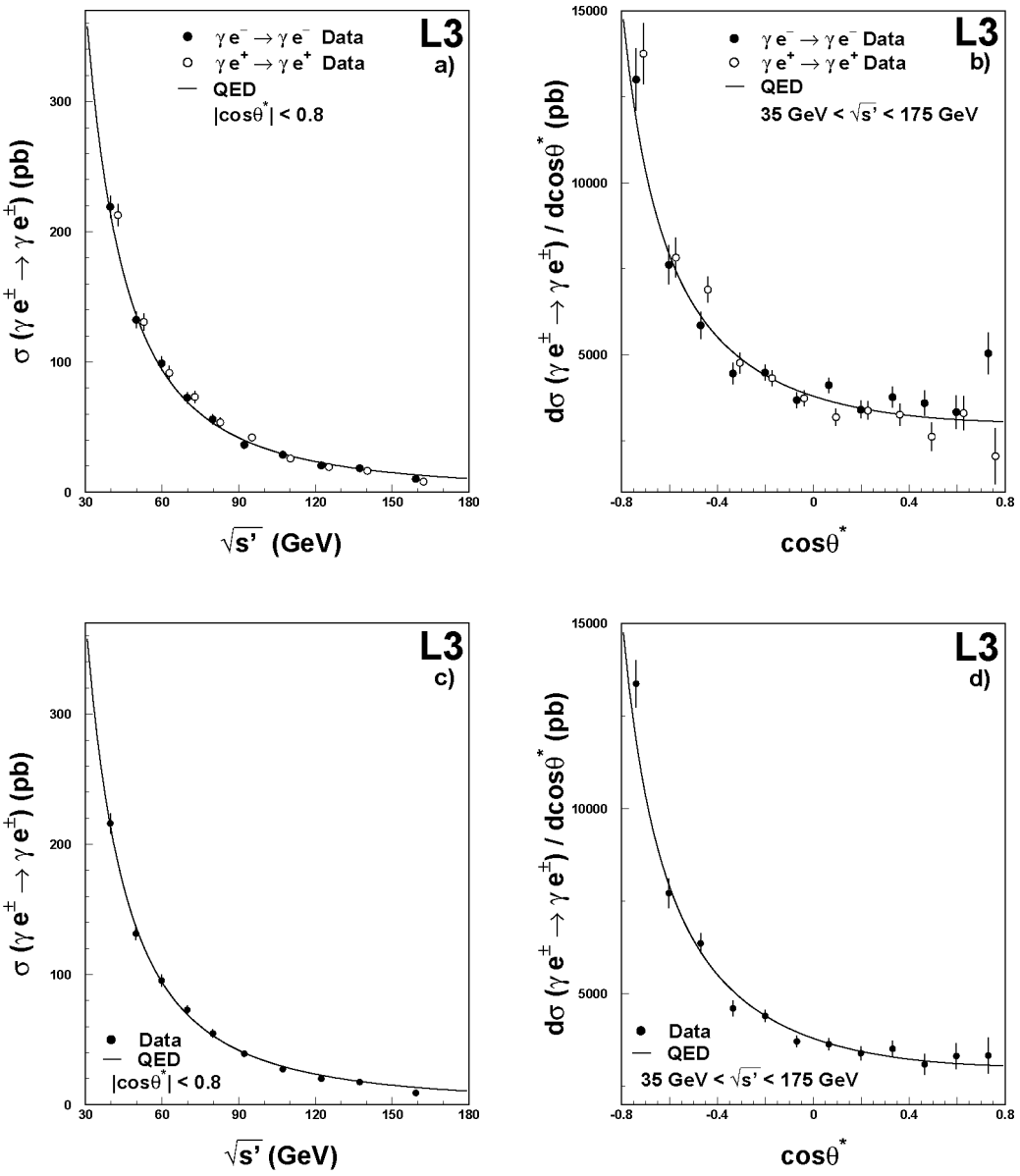

Figure 6: Measured cross sections of the $\gamma e^+ \to \gamma e^+$, $\gamma e^- \to \gamma e^-$ and $\gamma e^\pm \to \gamma e^\pm$ process as a function of a) and c) the effective centre-of-mass energy for $|\cos\theta^*| < 0.8$ and b) and d) the rest-frame scattering angle for $\sqrt{s'} = 35 - 175$ GeV. For clarity, the measurements for positrons in a) and b) are slightly displaced to the right. Data collected at e^+e^- centre-of-mass energies $\sqrt{s} = 188.6 - 209.2$ GeV are considered and the QED predictions are also shown.

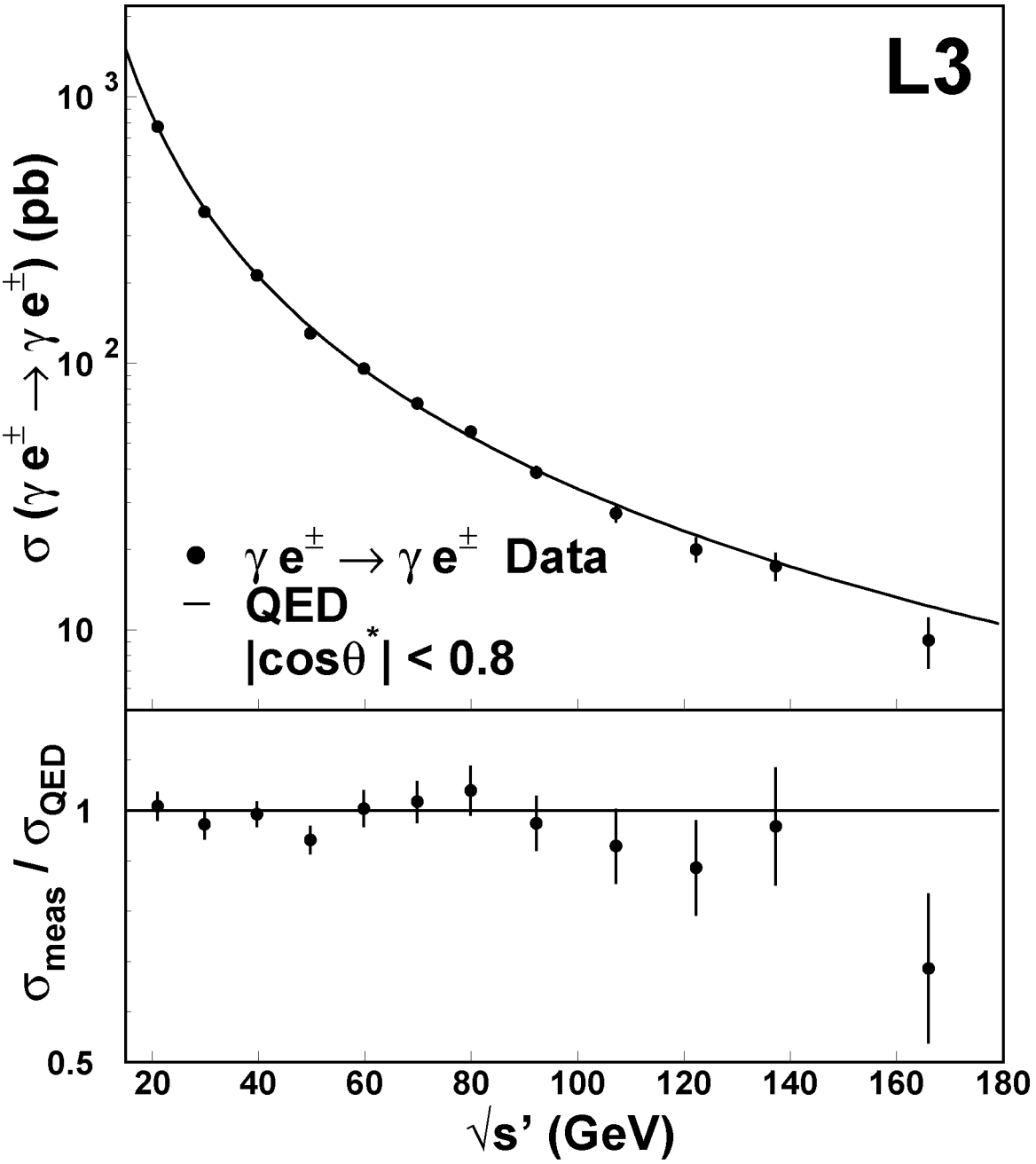

Figure 7: Cross section of the $\gamma e^{\pm} \to \gamma e^{\pm}$ process measured as a function of the effective centre-of-mass energy, $\sqrt{s'}$, for $|\cos\theta^*| < 0.8$, compared to the QED predictions. The full data sample collected at $\sqrt{s} = 91.2 - 209.2$ GeV is considered and the cosine of the electron rest-frame scattering angle is limited to the range $|\cos\theta^*| < 0.8$.